Exciton-phonon coupling in InP quantum dots with ZnS and (Zn, Cd) Se shells

Annalisa Brodu,[1] Mariana V. Ballottin,[2] Jonathan Buhot [ORCID],[2] Dorian Dupont,[3,4] Mickael Tessier,[3,4] Zeger Hens,[3]
Freddy T. Rabouw,[1] Peter C. M. Christianen,[2] Celso de Mello Donega [ORCID],[1] and Daniel Vanmaekelbergh[1,*]

[1]*Debye Institute for Nanomaterials Science, Utrecht University, The Netherlands*
[2]*High Field Magnet Laboratory, HFML-EMFL, Radboud University, Nijmegen, The Netherlands*
[3]*Physics and Chemistry of Nanostructures, Ghent University, Belgium*
[4]*SIM-Flanders vzw, Zwijnaarde, Gent, Belgium*

InP-based colloidal quantum dots are promising for optoelectronic devices such as light-emitting diodes and lasers. Understanding and optimizing their emission process is of scientific interest and essential for large-scale applications. Here we present a study of the exciton recombination dynamics in InP QDs with various shells: ZnS, ZnSe, and (Zn,Cd)Se with different amounts of Cd (5, 9, 12%). Phonon energies extracted from Raman spectroscopy measurements at cryogenic temperatures (4–5 K) are compared with exciton emission peaks observed in fluorescence line narrowing spectra. This allowed us to determine the position of both the bright $F = \pm 1$ state and the lowest dark $F = \pm 2$ state. We could identify the phonon modes involved in the radiative recombination of the dark state and found that acoustic and optical phonons of both the core and the shell are involved in this process. The Cd content in the shell increases electron wave-function delocalization, and thereby enhances the exciton-phonon coupling through the Fröhlich interaction.

I. INTRODUCTION

Colloidal semiconductor nanocrystals (NCs) exhibit size-tunable narrow emission spectra in combination with broad absorption and excitation spectra. These characteristics make colloidal semiconductor NCs (often called quantum dots, QDs) of high interest in nanoscience and optoelectronic applications, such as lasers and light-emitting diodes (LEDs) [1–7]. InP-based QDs have a high potential for optoelectronics because of their bright emission, ranging from 500 to 1000 nm [8,9], with near-unity photoluminescence quantum yield [10]. The promise of large-scale applications of InP-based QDs requires a detailed optical characterization to determine the exciton recombination processes, including the exciton-phonon interaction.

In recent years, several studies have established that in II–VI semiconductor nanomaterials with zincblende structure and prolate shape, the degeneracy of the lowest exciton level is partially lifted due to the electron-hole exchange interaction and the shape asymmetry of the QDs [11–16]. This results in an exciton fine structure that consists of five levels. The lowest-energy exciton state is referred to as a dark state because radiative recombination from it is forbidden within the electric-dipole approximation. This state is followed by a higher-energy "bright" exciton state from which the radiative transition to the ground state is allowed [15,16].

Several studies have reported effects of exciton-phonon coupling on the emission from the different exciton fine-structure levels. While most such studies focused on core-only

QDs [17–21], core/shell QDs are more relevant for applications. Usually in a core/shell geometry, a higher band-gap material overcoats the core to protect it from fast oxidation and to increase the photoluminescence quantum yield by passivating surface defects. The shell can play a fundamental role in the exciton radiative recombination process. For instance, in core/shell QDs the electron (e) and hole (h) wave functions can be both localized in the core (type-I localization regime), or be spatially separated in the core and shell (type-II localization regime). An intermediate regime (type-I$^{1/2}$), in which one carrier is localized while the other is delocalized over the whole QD, is also possible [22]. In this way, the carrier localization regime can be tuned from type I to type II, which has important consequences for the exciton fine structure [14] and a number of properties, for example the photoluminescence (PL) and absorption spectra, phonon coupling, and blinking mechanism [9,22–26]. When the e- and h wave functions are (partially) spatially separated (type-I½ or type-II regime), the exciton is polarized which increases coupling to lattice phonons via the Fröhlich interaction [27–29]. Despite the relevance of this, thorough studies of the exciton-phonon coupling in core/shell structures remain scarce.

Here, we present a study of the exciton-phonon coupling in InP-based QDs with various shells: ZnS, ZnSe, and (Zn,Cd)Se with different amounts of Cd (5, 9, 12%). All samples have an InP QD core diameter of 3.0 ± 0.1 nm while the total diameters of the QDs range from 4 ± 1 nm for the InP/ZnS sample to 14 ± 1 nm for the InP/(Zn,Cd)Se shells. The PL quantum yields of all samples are around 60% and decrease by a few percent with increasing Cd content [8,23]. We studied the exciton-phonon coupling using a combination of Raman spectroscopy and fluorescence line-narrowing (FLN)

---

*Corresponding author: d.vanmaekelbergh@uu.nl

spectroscopy at 4 K. Raman spectra reveal the phonon energies in these core/shell structures. FLN spectra show multiple emission peaks due to various emission pathways, which we assign to the involvement of several phonon modes.

We discuss the exciton states involved in the photoluminescence and the role of phonons in the recombination dynamics. Both acoustic and optical phonons of the core and shell are involved in the exciton recombination process and they play an important role in enhancing the radiative recombination rate of the dark state.

II. RESULTS AND DISCUSSION

A. Sample characterization

We studied five InP core/shell QD samples with comparable InP core of 3.0 ± 0.1 nm in diameter and various shells: ZnS, ZnSe, and (Zn,Cd)Se with different Cd contents (5, 9, 12%). The InP QDs with ZnS and ZnSe shell were synthesized as described in Ref. [8], and the ones with (Zn,Cd)Se shell as described in Ref. [23]. The samples were characterized by PL spectroscopy at room temperature (RT) and at 4 K (Supplemental Material, Figure S1 [30]). All samples emit in the visible range between 1.92 and 2.06 eV at RT, with the InP/ZnS QDs emitting at 1.99 eV, the InP/ZnSe QDs emitting at 2.06 eV, while the PL peak of the InP/(Cd,Zn)Se QDs shifts to lower energies with increasing Cd content, reaching 1.92 eV for 12% Cd. These spectral shifts are easily understood in terms of carrier localization, which changes from the type-I regime for InP/ZnS and InP/ZnSe to (type-I$^{1/2}$) with a delocalized electron for InP/(Cd,Zn)Se [23]. The full width at half maximum (FWHM) of the PL peaks ranges from 150 to 180 meV. The PL spectra show a considerable blueshift (about 60 meV for all samples) upon cooling to 4 K, due to the contraction of the crystal lattice [31]. The PL blueshift is accompanied by a decrease in the FWHM which ranges from 130 to 150 meV at 4 K.

B. Raman and fluorescence line narrowing spectroscopy

We performed Raman spectroscopy to detect (Raman-active) phonons in the various InP core/shell QDs involved in this study. The phonon energies extracted from the Raman spectra were subsequently compared to results obtained from FLN spectroscopy, a size-selective technique that allows the observation of PL lines with reduced inhomogeneous line broadening. In FLN spectroscopy, a spectrally narrow laser line with energy matching the low-energy side of the absorption spectrum is used to resonantly excite a small subensemble of the QDs. More precisely, we used a laser with a linewidth of ~ 300-μeV FWHM, which is narrow compared to the inhomogeneously broadened QD spectrum (150-meV FWHM; see Fig. S1) or even the homogeneously broadened single-QD spectrum measured in our previous work (3-meV FWHM [32]). By exciting on the low-energy side of the absorption spectrum, only the QDs with a high oscillator strength exciton state (bright state) that matches the energy of the excitation photons are excited. This size-selective excitation results in a minimally inhomogeneously broadened emission spectrum, revealing the fine structure of the lowest exciton states and their coupling to phonons. This allowed
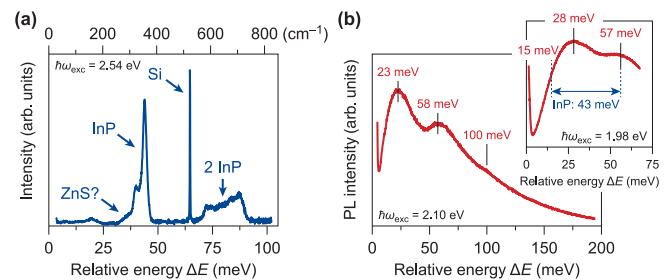
FIG. 1. Raman and FLN spectra recorded at 4 K for InP/ZnS core/shell QDs with a core diameter of 3.0 ± 0.1 nm. (a) Raman spectrum, obtained upon excitation at 2.54 eV. The peaks in the 300–400-cm^{-1} range are assigned to the LO and TO phonon modes of the InP cores. (b) FLN spectrum of the same InP/ZnS core/shell QD sample, obtained by exciting resonantly at 2.10 eV. Inset: High-resolution FLN spectrum of the same sample, obtained by exciting resonantly at 1.98 eV and detected by a triple-grating spectrometer. The laser energy (excited-state energy) is taken as reference and set to 0 meV, and the emission intensity is plotted as a function of $\Delta E = E_{\text{laser}} - E_{\text{detected}}$. The highest-intensity peak is related to emission from the dark state coupled to an acoustic phonon; the lower-intensity peaks are related to optical phonon replicas of the dark state.

us to study the exciton-phonon coupling in our systems [21]. To reduce the thermal broadening contribution, the FLN and Raman measurements were performed at 4 K.

C. Phonons in InP/ZnS QDs

Figure 1(a) presents the Raman spectrum of the InP/ZnS core/shell QDs recorded at 4 K, exciting the sample at 2.54 eV. It shows two peaks (fitting in Supplemental Material, Fig. S2 [30]) at 324 and 355 cm^{-1} (40 and 44 meV), which can be assigned to the transverse-optical (TO) and longitudinal-optical (LO) phonon modes of InP. These two peaks are shifted to higher energies compared to LO and TO phonon modes of the bare InP QDs (respectively, 310 and 342 cm^{-1}) [33,34], presumably due to the compressive strain created by the lattice mismatch with the ZnS shell, since the lattice parameter of ZnS is smaller than that of InP (viz., 5.420 and 5.869 Å, respectively, at 300 K). Similar results have been reported for InP QDs with CdSe and ZnSe shells [16,24]. The sharp peak at approximately 520 cm^{-1} originates from the crystalline silicon substrate [35]. At about 550–750 cm^{-1} double-Raman processes of the InP phonons are observed [marked as 2 InP in Fig. 1(a)]. No clear signature of ZnS phonons is observed between 275 and 350 cm^{-1} such as in the bulk material [36]. However, a bump around 250–300 cm^{-1} may be assigned to ZnS phonon modes. The absence of clear ZnS-related peaks is possibly due to the limited thickness of the ZnS shell, combined with partial overlap with the InP phonon peaks. We believe that the weak features below 200 cm^{-1} are associated with phonon modes related to the InP lattice, considering they are also present in the InP/ZnSe spectrum (see below and Supplemental Material, Fig. S3 [30]).

Figure 1(b) shows the low-temperature (4 K) FLN spectrum of the InP/ZnS core/shell QDs, excited resonantly at 2.10 eV. The inset is the high-resolution FLN spectrum of
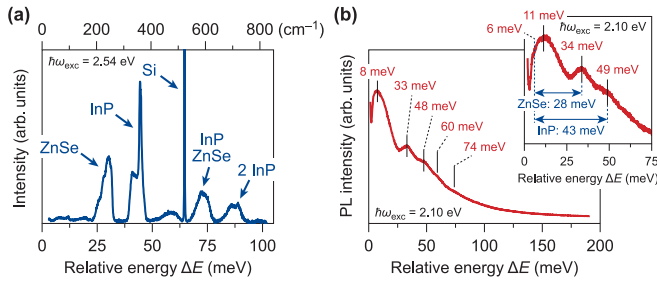
FIG. 2. Raman and FLN spectra recorded at 4 K for InP/ZnSe core/shell QDs with a core diameter of 3.0 ± 0.1 nm. (a) Raman spectrum, obtained upon excitation at 2.54 eV. The peaks in the 300–400- cm^{-1} range are assigned to the LO and TO phonon modes of the InP core in the InP/ZnSe core/shell QDs. The group of peaks around 200–260 cm^{-1} is assigned to the ZnSe phonon modes. (b) FLN spectrum of the same InP/ZnSe core/shell QD sample. Inset: High-resolution FLN spectrum of the same sample, detected by a triple-grating spectrometer. The spectra are obtained by exciting resonantly the sample at 2.10 eV. This excited state (2.10 eV) is taken as reference and set to 0 meV, and the emission intensity is plotted as a function of $\Delta E = E_{laser} - E_{detected}$. The highest-intensity peak is related to emission from the dark state coupled to an acoustic phonon; the lower-intensity peaks are related to optical phonon replicas of the ZnSe shell (28 meV) and the InP core (43 meV). The energies of phonon modes involved are indicated.

FIG. 3. Raman and FLN spectra recorded at 4 K for InP/ZnSe and InP/(Cd, Zn)Se core/shell QDs with the same InP core diameter of 3.0 ± 0.1 nm. (a) Raman spectra obtained upon excitation at 2.54 eV of InP/ZnSe core/shell QDs (green), and InP/(Cd, Zn)Se core/shell QDs with 5% of Cd (blue) and with 9% of Cd (purple). This measurement was performed in perpendicular polarization configuration, which rejects Raman scattering with the same polarization as the excitation beam (see Supplemental Material, Fig. S3 [30]). This explains why these spectra show no Si Raman peak. For clarity, curves have been shifted vertically and the most intense peaks are not fully shown. (b) FLN spectrum of the InP/(Cd, Zn)Se core/shell QDs with 9% of Cd, obtained upon resonant excitation at 2.07 eV. The inset shows the corresponding high-resolution spectrum upon excitation at 2.06 eV. The emission intensity is plotted as a function of $\Delta E = E_{laser} - E_{detected}$. The phonon energies involved are indicated.

the same sample, obtained by exciting the sample at 1.98 eV. The FLN spectra are referred to the energy of the excitation laser, which means that the energy of the excited state populated by the laser is taken as a reference and set to 0 meV. Two pronounced peaks are resolved at 23 and 58 meV from the laser line. A third less-defined feature is visible around 100 meV. The highest-intensity peak at 23 meV is ascribed to emission from the dark state coupled to acoustic phonons [16], while the lower-intensity peak at 58 meV is attributed to a vibronic replica due to coupling of the dark state with InP LO/TO phonons. The feature in the FLN spectrum at about 100 meV is assigned to a two-phonon replica due to coupling to the LO/TO phonon modes of InP. Although the zero-phonon line (ZPL) of the dark state is not resolved in the spectra, its position may be estimated by subtracting the InP phonon energy of 43 meV from the resonance peak observed at 58 meV, which yields 15 meV.

D. Phonons in InP/ZnSe QDs

In Fig. 2 we study the phonons involved in the excitonic recombination process in InP/ZnSe QDs. The Raman spectrum in Fig. 2(a), obtained under 2.54-eV excitation, shows peaks between 200 and 260 cm^{-1} (25–32 meV) that are absent in the Raman spectra of InP/ZnS QDs [see Fig. 1(a)]. We attribute these peaks to ZnSe phonons [16,24,37]. The LO and TO phonon modes of the InP lattice are present, also in this case, in the spectral range between 315 and 380 cm^{-1} (39–47 meV). Above 400 cm^{-1} it is possible to identify double-Raman and combination Raman processes of the InP and ZnSe phonons: the double mode of ZnSe lattice at approximately 470 cm^{-1}, the combination band of InP and ZnSe phonons at 590 cm^{-1}, and the double mode of InP lattice (plus possible contributions from the third overtone of ZnSe

phonon mode) between 650 and 750 cm^{-1}. The weak peaks below 200 cm^{-1} are associated with phonon modes of the InP lattice (see Supplemental Material, Fig. S3 [30]). In particular they can be ascribed to single process of acoustic phonon modes of InP due to an increase of the density of states in the center of the Brillouin zone (Γ) possibly created by defects in the crystal structure and a consequent backfolding of the phonon dispersion curves towards Γ [33,38] or to double processes at the edge of the Brillouin zone where the density of states may be strong. As mentioned above, the sharp peak at approximately 520 cm^{-1} comes from the phonon modes of the crystalline silicon substrate [35].

Figure 2(b) displays the FLN spectrum of the same InP/ZnSe QD sample excited at 2.10 eV. The highest-intensity peak (at around 8 meV from the laser line) is assigned to emission from the dark state coupled to acoustic phonons, as previously done in Ref. [16]. The peaks at 33 and 48 meV are attributed to vibronic replicas due to coupling of the dark state with a ZnSe and InP optical phonon, respectively. Furthermore, two weaker features, around 60 and 74 meV, are visible. These energy values match with a coupling of the dark state with two ZnSe phonons or with one InP and one ZnSe phonon, respectively. By subtracting the ZnSe phonon energy of 28 meV from the peak at 33 meV, or the InP phonon energy of 43 meV from the peak at 48 meV, we find a value of 5 meV for the ZPL. Interestingly, a weak hump is observed at 5–6 meV in the high-resolution FLN spectrum [inset in Fig. 2(b)] which can thus be assigned to the ZPL.

E. Phonons in InP/(Cd, Zn)Se QDs

Figure 3(a) presents the Raman spectra of InP/ZnSe core/shell QDs, and InP/(Cd, Zn)Se with 5 and 9% Cd, obtained under 2.54-eV excitation. A strong resonant effect
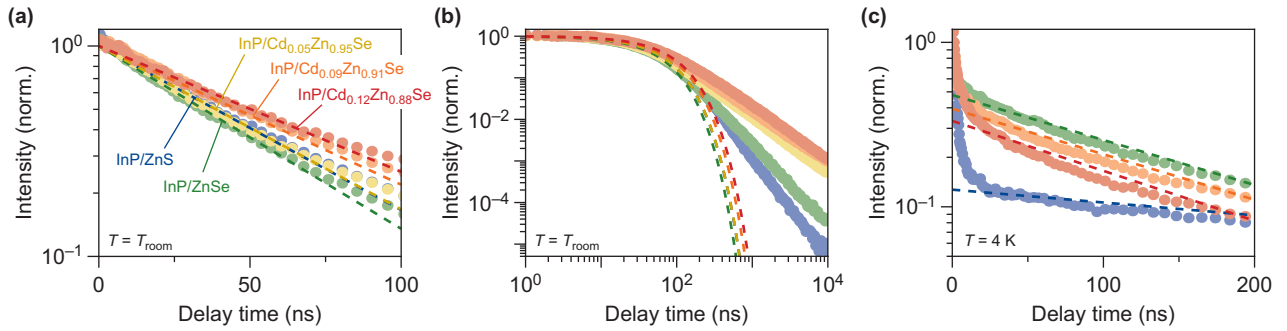
FIG. 4. PL decay curves measured at the PL peak maximum for the InP/ZnS QDs (blue), InP/ZnSe QDs (green), and InP/(Cd,Zn)Se core/shell QDs with 5% Cd (yellow), 9% Cd (orange), and 12% Cd (red). We used different detection energies for the different samples to match the PL peak maximum, which depends on shell composition and temperature as shown in Fig. S1. Dashed lines are fits to single-exponential decay. (a) PL decay curves measured at room temperature and plotted on a semilogarithmic scale. (b) The same PL decay curves, but plotted on a double-logarithmic scale up to a delay time of $10\,\mu$s. (c) PL decay curves measured at 4 K at the peak maximum (which is shifted compared to room temperature) and plotted on a semilogarithmic scale.

is observed in the Raman-scattering peaks of the samples with Cd-containing shells, which has previously been studied in Ref. [24]. As a consequence of this strong resonance, an impressive series of overtones is observed for the shells with 5 and 9% of Cd. Their appearance is due to a closer energy match of the shell band gap and the excitation energy with increasing Cd content. The energy of the phonon modes of the shell around 200–260 cm^{-1} does not significantly change when Cd is mixed into the ZnSe material (up to 9%), as was observed previously [24]. Contrary to the strongly enhanced Raman-scattering signal from shell phonons, the signal from InP core phonons decreases with Cd doping and is hardly observable for the QDs with 9% Cd shell. Similarly to the shell phonons, the energy of InP core phonons is not significantly affected by composition of the (Cd,Zn)Se shell [24].

We compare the phonon energies extracted from the Raman spectra with the positions of the FLN peaks of the InP/(Cd, Zn)Se QDs sample with 9% Cd [Fig. 3(b)]. The FLN peak energies are comparable to those observed for the InP/ZnSe QDs sample [Fig. 2(b)], but the phonon replicas are better defined. In the FLN spectrum of the sample with 9% Cd, we even observe an indication of a two-InP phonon replica at approximately 90 meV from the laser line. Furthermore, a small peak at approximately 5 meV is observed and ascribed to the ZPL. The energy difference from this ZPL to the peaks at 33 meV and at 48 meV matches perfectly with the phonon energies of the (Cd,Zn)Se shell and the InP core, respectively.

F. Photoluminescence decay of InP/ZnS, InP/ZnSe and InP/(Cd,Zn)Se core/shell QDs

Figure 4(a) shows the PL decay curves of our samples measured at the PL peak maximum at room temperature for the InP/ZnS QDs (blue), InP/ZnSe QDs (green), and InP/(Cd,Zn)Se core/shell QDs with 5% Cd (yellow), 9% Cd (orange), and 12% Cd (red). On a short timescale up to 100 ns, the curves are nearly single exponential with lifetimes of approximately 50 ns. This initial fast decay is ascribed to the exciton radiative recombination, which involves the bright and dark exciton fine-structure states in thermal

equilibrium [15,16,39]. The radiative recombination rate is proportional to the square of the spatial overlap integral of the electron and hole wave functions [14,40,41]. Therefore, a reduction of the spatial overlap affects the oscillator strength of the exciton transitions and, accordingly, the radiative decay rates [14].

Using a single-exponential fit on the timescale from 0 to 100 ns, we estimate a radiative lifetime of $\tau = 55.7 \pm 0.8$ ns for the InP/ZnS QDs, and increasing lifetimes of $\tau = 50.0 \pm 0.7$, 55.9 ± 0.8, 65.9 ± 0.8, and 72.6 ± 1.2 ns for the InP/(Cd,Zn)Se QDs with increasing Cd content of 0, 5, 9, and 12%, respectively. The uncertainties in the fitted values are provided as ± 1 standard error. This lengthening of the exciton radiative lifetime suggests that the electron-hole wave-function overlap in InP/(Cd,Zn)Se QDs gradually decreases as the Cd content in the shell increases. This can be attributed to the increasing delocalization of the electron wave function into the shell due to the gradual reduction of the conduction-band offset with increasing Cd content. Indeed, admixing 12% Cd into a ZnSe shell shifts the conduction band edge by an estimated 100 meV [23].

Figure 4(b) presents the same PL decay curves at room temperature, plotted on a double logarithmic scale until $10\,\mu$s after excitation. On the timescale beyond 100 ns, the PL decay curves deviate from the single exponent that we fitted in Fig. 4(a) (dashed lines), and the emission is dominated by a "delayed component" with approximately power-law decay (i.e., straight line on double-logarithmic scale). This delayed component is assigned to temporary charge trapping (for example on the surface or at the core-shell heterointerface of the QD) for up to a few microseconds, until the exciton state is restored by detrapping and then emits a photon [42]. The contribution of the delayed emission (and hence the probability of temporary charge-carrier trapping) is smallest in the InP/ZnS QDs and increases with increasing Cd content for the InP/(Cd,Zn)Se QDs. This trend might be related to the larger shell thickness of QDs with higher Cd content (with a consequent increase of average number of traps per QD) or to the additional electron wave function delocalization into the shell. A similar behavior was found for CdSe/CdS QDs with increasing CdS shell thickness [42].

Figure 4(c) shows the PL decay curves of our samples at 4 K. The decay curves show a fast component at $t < 25$ ns, which we ascribe to emission from higher-energy (bright) states shortly after the laser pulse and prior to thermalization [14–16,42–46]. The slower decay from 50 to 200 ns is ascribed to radiative recombination from (mostly) the dark exciton state. Whereas at room temperature the lowest bright and dark exciton fine-structure states are both populated at thermal equilibrium, at 4 K the dark state dominates the thermal population distribution. The radiative lifetime is therefore significantly longer than at room temperature. This is evident when comparing Figs. 4(a) and 4(c). We estimate the radiative lifetimes at 4 K from a single-exponential fit of the PL decay curves, excluding the initial fast component. The largest reduction of the radiative recombination rates occurs for the InP/ZnS QD sample, as the lifetime increases by a factor of 10 from 55.7 ns at room temperature to 556 ns at 4 K.

Interestingly, the effect of the shell composition [i.e., ZnS vs (Cd,Zn)Se with increasing Cd content] on the radiative lifetimes at 4 K is opposite to that observed at room temperature. We find that the radiative lifetime at 4 K is by far the longest for the InP/ZnS QDs (viz., 556 ± 20 ns), and decreases from 159 ± 4 ns for the InP/ZnSe QDs to 157 ± 5 ns and 143 ± 6 ns for InP/(Cd,Zn)Se QDs with 9 and 12% Cd, respectively. This is in striking contrast to the behavior observed at room temperature, where the lifetime lengthens with increasing Cd content from 50 ns (no Cd) to 72.6 ns (12% Cd). These seemingly contradictory observations can nevertheless be both understood in terms of the effect of the shell composition on the delocalization of the electron wave function. As discussed above, the electron delocalization into the shell increases with increasing Cd content, due to the gradual reduction of the conduction-band offset between the InP core and the (Cd,Zn)Se shell. This is clearly reflected in the shift of PL peak to lower energies with increasing Cd content (viz., from 2.06 to 1.92 eV, from no Cd to 12% Cd), as a result of the reduction of the quantum confinement potential. At room temperature, the direct effect of the reduction of the electron-hole overlap integral on the exciton oscillator strength dominates because the emission originates primarily from the bright exciton fine-structure state. Consequently, the exciton radiative lifetime at room temperature lengthens with increasing Cd content. In contrast, at 4 K the emission comes predominantly from the dark exciton fine-structure state because the population of the bright-exciton state is negligible. Radiative recombination from the dark state is forbidden within the electric-dipole approximation, and therefore coupling to polar phonons is required to induce significant transition dipole moments, and hence enhance the radiative recombination rate [14,39,47,48]. The vibronic nature of the dark-exciton emission is clearly evidenced in the FLN spectra discussed above. As a result, the radiative recombination rate of the dark-exciton fine-structure state (and therefore the radiative lifetime at 4 K) is expected to be extremely sensitive to the exciton-phonon coupling strength. We argue that the dependence of the radiative lifetimes at 4 K on the shell composition can be rationalized in terms of the impact of the delocalization of the electron wave function on the exciton-phonon coupling. The gradual increase of the electron delocalization into the shell going from ZnS to

(Cd,Zn)Se with increasing Cd content leads to increasingly larger exciton polarizability, which enhances coupling to polar lattice phonons through the Fröhlich interaction, [18,27–29] as previously shown for type-I$^{1/2}$ and type-II CdTe/CdSe heteronanocrystals with increasing degree of electron-hole spatial separation [28]. This interpretation is consistent with the FLN data discussed above, which show more-pronounced phonon replicas for InP core/shell QDs when going from a ZnS [Fig. 1(b)] to a ZnSe [Fig. 2(b)] and to a (Cd,Zn)Se [Fig. 3(b)] shell.

III. CONCLUSION

We studied the exciton fine structure and the role of phonons in core/shell quantum dot systems with an InP core of around 3.0 ± 0.1 nm and various shells: ZnS, ZnSe, and (Zn,Cd)Se. In particular, the phonon energies extracted from Raman spectra were compared with the peak positions in fluorescence line narrowing spectra at $T = 4$ K. Our results demonstrate how the lower bright-and dark-exciton fine-structure states are involved in the exciton radiative recombination and the dynamic and crucial role of phonons in activating the emission from the dark state. We find that the exciton recombination process involves acoustic and optical phonons of both the core and the shell. The coupling to phonons plays a major role in the recombination process increasing the oscillator strength of the dark state [14,39,47,48] and hence enhancing the radiative recombination rates. This broadens the dark-exciton emission spectra of InP-based QDs at the single-QD level. The impact of this on InP emission spectra for room-temperature applications with inhomogeneously broadened ensembles remains to be determined.

IV. METHODS

A. Sample preparation

InP/ZnS and InP/ZnSe core/shell QD samples were synthesized, following the method reported in Ref. [8]. InP QDs with (Zn,Cd)Se shell were synthesized following the method of Ref. [23]. The QD samples were washed by precipitation with methanol, isolated by centrifugation, and redispersed in toluene and 1-dodecanethiol. To achieve a QD film the solution was deposited using a drop-cast method, on crystalline silicon substrate for Raman and FLN measurements, and on a quartz substrate for PL and time-resolved photoluminescence (TrPL) measurements.

B. PL and TrPL

The PL and the time-resolved PL measurements were performed on QD films deposited on quartz substrates (see Sample Preparation above). In the PL measurements, the excitation was provided by a 450-W xenon lamp and the PL signal was dispersed by an Edinburgh Instruments FLS920 spectrometer equipped with double-grating monochromators and detected by a Hamamatsu R928 photomultiplier tube (PMT).

The time-resolved PL decay measurements were performed monitoring the PL peak wavelength for all samples. The excitation was provided by a pulsed diode laser, operating

at 405 nm with a repetition rate of 100 kHz. The instrument response function of the entire setup has a width of approximately 500 ps, much narrower than the fastest dynamics we studied in Fig. 4. The time-resolved PL curves were acquired by time-correlated single-photon counting using a Hamamatsu H7422 PMT. The count rate was kept at 3% of the laser repetition rate, by adjusting the slit width between 1 and 5 nm. This low excitation fluence was used in order to maintain single-photon statistics and avoid multiexciton formation.

To achieve low temperatures, samples were placed inside an optical ^{4}He cryostat (Oxford Instruments).

C. Raman spectroscopy measurements

Raman-scattering measurements were performed at High Field Magnet Laboratory (Radboud University). To achieve low temperatures, samples were placed in an optical ^{4}He cryostat (Microstat Oxford). Samples were probed in backscattering geometry with an incident laser line at 488 nm from a solid-state laser. To prevent both excessive laser heating and sample damage, a low laser power of 30 μW was used. The scattered light was filtered by a RazorEdge ultrasteep long-pass edge filter and analyzed by a 1-m-long single grating (1200 grooves/m-m) FHR-1000 Horiba spectrometer equipped with a nitrogen-cooled PyLoN charge-coupled device (CCD) camera (Princeton Instruments). The resolution of our measurements was 1 cm^{-1}.

D. Fluorescence line-narrowing measurements

FLN experiments at low temperatures were performed at the High Field Magnet Laboratory (Radboud University). For these experiments the samples used were QD films on crystalline silicon substrate (see Sample Preparation). To achieve low temperatures, the samples were placed in an optical ^{4}He cryostat (Microstat Oxford). Samples were probed in backscattering geometry. The FLN measurements were performed using a narrow excitation source, achieved by using a tunable jet-stream dye (Rhodamine 6G) laser. This monochromatic laser beam was circularly polarized by means of a linear polarizer and a Babinet-Soleil compensator. The FLN signal was guided through a 0.3-m-long single-grating spectrometer (300 grooves/mm grating) and detected by a liquid-nitrogen-cooled CCD. The emitted photons were detected in crossed polarization relative to the laser polarization by using a linear polarizer and a lambda quarter-wave plate. Cutoff optical filters were used in excitation and detection.

For the high-resolution FLN spectra, the samples were mounted in a titanium sample holder on top of a three-axis piezopositioner. The laser beam was focused on the sample by a singlet lens (10-mm focal length). The same lens was used to collect the PL emission and direct it to the detection setup (backscattering geometry). The samples and optical probe were mounted inside a liquid-helium bath cryostat. The high-resolution FLN emission was detected in crossed polarization mode relative to the laser polarization by using a linear polarizer and a lambda quarter-wave plate. The resonant-PL emission was analyzed by a 0.5-m-long triple-grating spectrometer (three 1800 grooves/mm holographic gratings) in subtractive mode, equipped with a liquid-nitrogen-cooled CCD camera (Symphony-Horiba).

[1] M. Grundmann, Phys. E Low-Dimensional Syst. Nanostruct. **5**, 167 (1999).

[2] N. N. Ledentsov, Semicond. Sci. Technol. **26**, 014001 (2011).

[3] I. Samuel, Nat. Mater. **17**, 9 (2017).

[4] E. Jang, S. Jun, H. Jang, J. Lim, B. Kim, and Y. Kim, Adv. Mater. **22**, 3076 (2010).

[5] T.-H. Kim, S. Jun, K.-S. Cho, B. L. Choi, and E. Jang, MRS Bull. **38**, 712 (2013).

[6] D. V. Talapin and J. Steckel, MRS Bull. **38**, 685 (2013).

[7] G. J. Supran, Y. Shirasaki, K. W. Song, J.-M. Caruge, P. T. Kazlas, S. Coe-Sullivan, T. L. Andrew, M. G. Bawendi, and V. Bulović, MRS Bull. **38**, 703 (2013).

[8] M. D. Tessier, D. Dupont, K. De Nolf, J. De Roo, and Z. Hens, Chem. Mater. **27**, 4893 (2015).

[9] R. Toufanian, A. Piryatinski, A. H. Mahler, R. Iyer, J. A. Hollingsworth, and A. M. Dennis, Front. Chem. **6**, 1 (2018).

[10] Y. Li, X. Hou, X. Dai, Z. Yao, L. Lv, Y. Jin, and X. Peng, J. Am. Chem. Soc. **141**, 6448 (2019).

[11] M. Nirmal, D. J. Norris, M. Kuno, M. G. Bawendi, A. L. Efros, and M. Rosen, Phys. Rev. Lett. **75**, 3728 (1995).

[12] A. L. Efros, M. Rosen, M. Kuno, M. Nirmal, D. J. Norris, and M. Bawendi, Phys. Rev. B **54**, 4843 (1996).

[13] J. H. Blokland, V. I. Claessen, F. J. P. Wijnen, E. Groeneveld, C. de Mello Donegá, D. Vanmaekelbergh, A. Meijerink, J. C. Maan, and P. C. M. Christianen, Phys. Rev. B **83**, 035304 (2011).

[14] A. Granados del Águila, E. Groeneveld, J. C. Maan, C. de Mello Donegá, and P. C. M. Christianen, ACS Nano **10**, 4102 (2016).

[15] L. Biadala, B. Siebers, Y. Beyazit, M. D. Tessier, D. Dupont, Z. Hens, D. R. Yakovlev, and M. Bayer, ACS Nano **10**, 3356 (2016).

[16] A. Brodu, M. V. Ballottin, J. Buhot, E. J. Van Harten, D. Dupont, A. La Porta, P. T. Prins, M. D. Tessier, M. A. M. Versteegh, V. Zwiller, S. Bals, Z. Hens, F. T. Rabouw, P. C. M. Christianen, C. De Mello Donega, and D. Vanmaekelbergh, ACS Photonics **5**, 3353 (2018).

[17] O. I. Micic, H. M. Cheong, H. Fu, A. Zunger, J. R. Sprague, A. Mascarenhas, and A. J. Nozik, J. Phys. Chem. B **101**, 4904 (1997).

[18] J. J. Shiang, S. H. Risbud, and A. P. Alivisatos, J. Chem. Phys. **98**, 8432 (1993).

[19] M. C. Klein, F. Hache, D. Ricard, and C. Flytzanis, Phys. Rev. B **42**, 11123 (1990).

[20] A. P. Alivisatos, T. D. Harris, P. J. Carroll, M. L. Steigerwald, and L. E. Brus, J. Chem. Phys. **90**, 3463 (1989).

[21] M. Nirmal, C. B. Murray, and M. G. Bawendi, Phys. Rev. B **50**, 2293 (1994).

[22] C. D. M. Donegá, Chem. Soc. Rev. **40**, 1512 (2011).

[23] D. Dupont, M. D. Tessier, P. F. Smet, and Z. Hens, Adv. Mater. **29**, 1700686 (2017).

[24] M. Rafipoor, D. Dupont, H. Tornatzky, M. D. Tessier, J. Maultzsch, Z. Hens, and H. Lange, Chem. Mater. **30**, 4393 (2018).

[25] H. Htoon, A. V. Malko, D. Bussian, J. Vela, Y. Chen, J. A. Hollingsworth, and V. I. Klimov, Nano Lett. **10**, 2401 (2010).

[26] A. M. Dennis, B. D. Mangum, A. Piryatinski, Y. S. Park, D. C. Hannah, J. L. Casson, D. J. Williams, R. D. Schaller, H. Htoon, and J. A. Hollingsworth, Nano Lett. **12**, 5545 (2012).

[27] C. Lin, K. Gong, D. F. Kelley, and A. M. Kelley, ACS Nano **9**, 8131 (2015).

[28] E. Groeneveld and C. De Mello Donegá, J. Phys. Chem. C **116**, 16240 (2012).

[29] J. Cui, A. P. Beyler, I. Coropceanu, L. Cleary, T. R. Avila, Y. Chen, J. M. Cordero, S. L. Heathcote, D. K. Harris, O. Chen, J. Cao, and M. G. Bawendi, Nano Lett. **16**, 289 (2016).

[30] See Supplemental Material at http://link.aps.org/supplemental/10.1103/PhysRevB.101.125413 for additional data including basic optical characterization of InP QD samples with different shells and more information on the Raman data analysis.

[31] K. Haruna, H. Maeta, K. Ohashi, and T. Koike, J. Phys. C Solid State Phys. **20**, 5275 (1987).

[32] A. Brodu, V. Chandrasekaran, L. Scarpelli, J. Buhot, F. Masia, M. V. Ballottin, M. Severijnen, M. D. Tessier, D. Dupont, F. T. Rabouw, P. C. M. Christianen, C. de Mello Donega, D. Vanmaekelbergh, W. Langbein, and Z. Hens, J. Phys. Chem. Lett. **10**, 5468 (2019).

[33] H. J. Hou and F. J. Kong, Phys. Status Solidi **248**, 1399 (2011).

[34] M. J. Seong, O. I. Mićić, A. J. Nozik, A. Mascarenhas, and H. M. Cheong, Appl. Phys. Lett. **82**, 185 (2003).

[35] Z. Q. Lu, T. Quinn, and H. S. Reehal, J. Appl. Phys. **97**, 033512 (2005).

[36] N. Vagelatos, D. Wehe, and J. S. King, J. Chem. Phys. **60**, 3613 (1974).

[37] U. Rössler, *New Data and Updates for Several Semiconductors with Chalcopyrite Structure, for Several II-VI Compounds and Diluted Magnetic IV-VI Compounds* (Springer, Berlin, 2013).

[38] E. G. Gadret, M. M. de Lima, J. R. Madureira, T. Chiaramonte, M. A. Cotta, F. Iikawa, and A. Cantarero, Appl. Phys. Lett. **102**, 122101 (2013).

[39] J. Eilers, J. Van Hest, A. Meijerink, and C. D. M. Donega, J. Phys. Chem. C **118**, 23313 (2014).

[40] C. de Mello Donegá and R. Koole, J. Phys. Chem. C **113**, 6511 (2009).

[41] A. L. Efros, Phys. Rev. B **46**, 7448 (1992).

[42] F. T. Rabouw, M. Kamp, R. J. A. van Dijk-Moes, D. R. Gamelin, A. F. Koenderink, A. Meijerink, and D. Vanmaekelbergh, Nano Lett. **15**, 7718 (2015).

[43] F. Liu, L. Biadala, A. V. Rodina, D. R. Yakovlev, D. Dunker, C. Javaux, J.-P. Hermier, A. L. Efros, B. Dubertret, and M. Bayer, Phys. Rev. B **88**, 035302 (2013).

[44] L. Biadala, Y. Louyer, P. Tamarat, and B. Lounis, Phys. Rev. Lett. **103**, 037404 (2009).

[45] L. Biadala, B. Siebers, R. Gomes, Z. Hens, D. R. Yakovlev, and M. Bayer, J. Phys. Chem. C **118**, 22309 (2014).

[46] D. Oron, A. Aharoni, C. de Mello Donega, J. van Rijssel, A. Meijerink, and U. Banin, Phys. Rev. Lett. **102**, 177402 (2009).

[47] C. Y. Wong, J. Kim, P. S. Nair, M. C. Nagy, and G. D. Scholes, J. Phys. Chem. C **113**, 795 (2009).

[48] V. M. Huxter and G. D. Scholes, J. Chem. Phys. **132**, 104506 (2010).